Nanoscale

PAPER

View Article Online
View Journal | View Issue

Cite this: *Nanoscale*, 2015, **7**, 6843

Europium-engineered iron oxide nanocubes with high T_1 and T_2 contrast abilities for MRI in living subjects†

Lijiao Yang,[a] Zijian Zhou,[a] Hanyu Liu,[a] Changqiang Wu,[b] Hui Zhang,[a] Guoming Huang,[a] Hua Ai[b] and Jinhao Gao*[a]

Received 3rd February 2015,
Accepted 14th March 2015

DOI: 10.1039/c5nr00774g

www.rsc.org/nanoscale

Magnetic resonance imaging (MRI) contrast agents with both positive (T_1) and negative (T_2) contrast abilities are needed in clinical diagnosis for fault-free accurate detection of lesions. We report a facile synthesis of europium-engineered iron oxide (EuIO) nanocubes as T_1 and T_2 contrast agents for MRI in living subjects. The Eu(III) oxide-embedded iron oxide nanoparticles significantly increase the T_1 relaxivity with an enhanced positive contrast effect. EuIO nanocubes with 14 nm in diameter showed a high r_1 value of 36.8 mM^{-1} s^{-1} with respect to total metal ions (Fe + Eu), which is about 3 times higher than that of Fe_3O_4 nanoparticles with similar size. Moreover, both r_1 and r_2 values of EuIO nanocubes can be tuned by varying their sizes and Eu doping ratios. After citrate coating, EuIO nanocubes can provide enhanced T_1 and T_2 contrast effects in small animals, particularly in the cardiac and liver regions. This work may provide an insightful strategy to design MRI contrast agents with both positive and negative contrast abilities for biomedical applications.

Introduction

Magnetic resonance imaging (MRI) has been widely used in the clinic owing to the noninvasive character and high spatial resolution in soft issue.[1–3] Magnetic nanomaterials are employed as contrast agents to improve the sensitivity and reliability of MRI by accelerating the proton relaxation of the nearby water molecules.[4,5] As a result, they are able to enhance the contrast of the region of interest from the background under external magnetic fields. There are two types of contrast agents, T_1 positive contrast agents (*e.g.*, Gd chelates, paramagnetic Gd_2O_3 and MnO nanomaterials),[6–9] and T_2 negative contrast agents (*e.g.*, superparamagnetic Fe_3O_4, $ZnFe_2O_4$ and Fe_5C_2 nanomaterials).[10–15] However, these single modal MRI contrast agents have high risk of pseudo-positive signals in diagnosing lesions due to the intrinsic background from tissues in their vicinity. For example, T_1-weighted MRI with bright signals may confuse with neighboring adipose tissues, whereas T_2-weighted MRI showing darker signals is not favorable for distinguishing tissues in some occasions.[16,17] Therefore, MRI contrast agents with both positive (T_1) and negative (T_2) contrast abilities are needed in clinical diagnosis for fault-free accurate detection of diseases. Ultrasmall iron oxide (IO) nanoparticles can display T_1–T_2 dual-modal MRI behavior because of strong surface spin-canting effect and low magnetization.[18,19] However, they usually show low relaxivities and worse still low stability in biological media,[20] which hinders the further applications as efficient T_1- and T_2-weighted MRI contrast agents.

Paramagnetic metals (*e.g.*, Mn^{2+}) promise highly efficient T_1 contrast due to the presence of unpaired electrons.[21–23] The doping of paramagnetic metals into iron oxide nanoparticles can achieve enhanced T_1 contrast and even tunable T_1–T_2 dual-modal contrasts in contrast-enhanced MRI applications.[24,25] There are also other strategies to construct dual modal MR imaging, such as combining T_1 and T_2 contrast agents together *via* hybrid heterostructures and designing a "magnetically decoupled" core–shell structure.[26,27] On the other hand, lanthanide (Ln) ions, such as Gd^{3+} with seven unpaired electrons, were employed to enhance the contrast abilities of iron oxide nanoparticles through the embedding strategy, which promises enhanced T_1 and T_2 contrast efficiency for sensitive and accurate MR imaging and disease diagnosis.[28–32] Therefore, Eu(III) ions with six unpaired electrons may hold great potential to regulate the MRI contrast

[a]*State Key Laboratory of Physical Chemistry of Solid Surfaces, The Key Laboratory for Chemical Biology of Fujian Province and Department of Chemical Biology, College of Chemistry and Chemical Engineering, Xiamen University, Xiamen 361005, China. E-mail: jhgao@xmu.edu.cn; Fax: +86-592-2189959; Tel: +86-592-2180278*
[b]*National Engineering Research Center for Biomaterials, Sichuan University, Chengdu 610064, China*

†Electronic supplementary information (ESI) available. See DOI: 10.1039/c5nr00774g

ability of iron oxide nanoparticles. Herein, we synthesized europium-engineered iron oxide (EuIO) nanocubes as novel MRI contrast agents and investigated the impact of Eu(III) ions on both T_1 and T_2 contrast abilities of iron oxide nanoparticles. The T_1 and T_2 relaxivities of EuIO nanocubes are size- and composition-dependent. EuIO nanocubes with larger size have higher r_1 and r_2 values. A high ratio of Eu embedding can increase r_1 values while reducing the r_2 values. EuIO nanocubes showed good biocompatibility and relatively long blood circulation time after coating with sodium citrate molecules. More importantly, the EuIO nanocubes can serve as enhanced T_1 and T_2 MRI contrast agents in living subjects using a clinically available 3.0 T MRI scanner, which may open up a new avenue to design high-performance MRI contrast agents for imaging and diagnosis applications.

Experimental section

Preparation of metal–oleate complex

A metal–oleate complex was prepared by reacting sodium oleate and metal chlorides following a typical modified method from the literature.[33] Briefly, 0.811 g of ferric chloride (5 mmol) and 4.567 g of sodium oleate (15 mmol) were dissolved in the solvent mixed with 20 mL ethanol, 15 mL distilled water and 30 mL hexane. The resulting mixture was heated to 70 °C and stirred for four hours. After cooling to room temperature, the upper layer containing iron–oleate was washed with distilled water three times. The resulting red-brownish iron–oleate complex in a waxy solid form was obtained after evaporating hexane. The europium–oleate complex (white powder) was produced in a similar way but using europium chlorides as precursors.

Preparation of monodispersed EuIO nanocubes

Monodispersed hydrophobic EuIO nanocubes were synthesized by thermal decomposition of metal–oleate complexes. For 14 nm EuIO nanocubes with a Eu molar ratio of 10.3%, iron–oleate (0.902 g, 1 mmol), europium–oleate (0.0996 g, 0.1 mmol), oleic acid (0.176 mL, 0.55 mmol) and 1-octadecene (15 mL) were mixed in a flask. The solution was heated to 350 °C at a constant rate of 5 °C min^{-1} under a nitrogen atmosphere, and maintained at the temperature for 1.5 hours. After cooling the solution to room temperature, isopropanol was added to precipitate the nanoparticles. The product was washed with ethanol three times, collected by centrifugation and finally redispersed in hexane for further use. The reflux time was one hour for 10 nm EuIO nanocubes and two hours for 20 nm EuIO nanocubes. We varied the ratios of europium–oleate and iron–oleate precursors to obtain EuIO nanocubes with different Eu molar ratios.

Preparation of 14 nm Fe_3O_4 and 14 nm Eu_2O_3 nanoparticles

For 14 nm monodispersed Fe_3O_4 nanoparticles, iron oleate (0.902 g, 1 mmol) and oleic acid (0.16 mL, 0.5 mmol) were added to a three neck bottle flask with 1-octadecene (12 mL) as the solvent. After reflux for 1.5 hours under a nitrogen atmosphere and cooling to room temperature, the nanoparticles were precipitated with isopropanol, then washed with ethanol, separated by centrifugation and redispersed in hexane for further use.

For 14 nm monodispersed Eu_2O_3 nanoparticles, europium oleate (0.996 g, 1 mmol) was dissolved in trioctylamine (10 mL) containing oleic acid (0.16 mL), the reaction was heated to reflux temperature and maintained for one hour. After cooling to room temperature, ethanol was added to precipitate the nanoparticles, and then the product was washed with ethanol and redispersed in hexane for further use.

Preparation of sodium citrate coated EuIO nanocubes

We choose sodium citrate as a phase transfer agent because it gives a much smaller hydrodynamic radius than polymeric ligands. 4 mL of EuIO nanocube hexane solution (containing 10 mg nanocubes) was mixed with 4 mL of distilled water including 60 mg of sodium citrate, the mixture was added to 6 mL acetone and heated at 70 °C for four hours. The products were collected by centrifugation after being cooled to room temperature. The EuIO nanocubes were then purified using sterilized membrane filters (pore size of 0.22 μm) for further use. The Fe_3O_4 and Eu_2O_3 nanoparticles were also coated with sodium citrate using similar methods.

Cytotoxicity assay

The cytotoxicity of the EuIO nanocubes (sodium citrate coating) was tested by the 3-(4,5-dimethylthiazol-2-y1)-2,5-diphenyltetrazolium bromide (MTT) method. SMMC-7721 or MRC-5 cells were firstly seeded into a 96-well plate with a density of 1×10^4 cells per well in RPMI 1640, and incubated in 5% CO_2 at 37 °C overnight. The cells were then incubated with 14 nm EuIO nanocubes at various [Fe + Eu] concentrations (0.469, 0.938, 1.875, 3.75, 7.5, 15, 30, 60 and 120 μg mL^{-1}) for 24 h and 48 h. Then the culture medium was removed, and each well was added 100 μL of the new culture medium containing MTT (0.5 μg mL^{-1}) and incubated for 4 h. The OD_{492} value (Abs.) of each well was measured using a MultiSkan FC microplate reader immediately. Cell viability was calculated from the OD_{492} value of the experimental group by subtracting that of the blank group.

Cell uptake study

The SMMC-7721 cells (1×10^6) were seeded in the dish for 12 h, after washing cells twice with PBS, we added 10 mL RPMI-1640 containing EuIO nanocubes and Fe_3O_4 nanoparticles with different concentrations (0.8, 0.4 and 0.2 mM of total metals, respectively) and incubated at 37 °C for 5 h. The cells were harvested and washed with PBS buffer three times to remove the free nanoparticles. Then we collected the cells in a 0.6 mL graduated centrifuge tube by centrifugation for MRI scanning. The MRI experiment was performed on a 0.5 T MRI scanner.

Relaxivity and MRI phantom studies at 0.5 T

All experiments were performed on a 0.5 T NMI20-Analyst NMR system (Niumag Corporation, Shanghai, China). A series of EuIO nanocubes, Fe_3O_4 and Eu_2O_3 nanoparticles were prepared with different concentrations (0.4, 0.2, 0.1, 0.05 and 0.025 mM) of total metals in 1% agar-containing solution. The control sample (0 mM) was manufactured with purified water containing 1% agar. We used an inversion recovery (IR) sequence and the Carr–Purcell–Meiboom–Gill (CPMG) sequence to measure the longitudinal relaxation times (T_1) and transverse relaxation times (T_2). The relaxivity values r_1 and r_2 were calculated from the slopes of the plot of $1/T_1$ or $1/T_2$ against the total metal concentration ([Fe + Eu], [Fe] or [Eu] in mM). T_1- and T_2-weighted phantom images were acquired by a 2D multi-slice spin-echo (MSE) sequence with the following parameters: TR/TE = 200/2 ms (T_1), TR/TE = 2000/40 ms (T_2), 512 × 512 matrices, and repetition times = 4.

In vivo MRI study

All the samples were filtered through sterilized membrane filters (pore size 0.22 μm) for further use. Healthy Sprague–Dawley rats weighing about 180–220 g were chosen for *in vivo* MRI studies. T_1-weighted MR images of the heart and T_2-weighted MR images of the liver were obtained on a Philips (Achieva 3.0 T) MRI scanner. The rats (for each group, n = 3) were intravenously injected 14 nm sized EuIO nanocubes with a dose of 2 mg (Eu + Fe) per kg of body weight. For T_1 imaging, time-scale acquisition of images was acquired at different time points (1 min, 3 min and 5 min) post-injection with the same slices. The images were obtained using a 3D CEMRA (contrast enhanced angiography) sequence under the following parameters: TR/TE = 7/3 ms, thickness = 1 mm, 1024 × 1024 matrices, FOV = 100 × 100 mm, flip angle = 30°. For T_2 imaging, the slices were further acquired at different time points (30 min, 90 min and 150 min) after the injection. The images were obtained using a fast spin-echo sequence (TSE) under the following parameters: TR/TE = 2000/66 ms, thickness = 1 mm, 144 × 144 matrices, FOV = 50 × 50 mm, flip angle = 90°. To quantify the contrast enhancement, the signal-to-noise ratio (SNR) was measured by analyzing regions of interest (ROIs) of the images, and the contrast enhancement was defined as the decrease of SNR after the injection, $\Delta SNR = (|SNR_{post} - SNR_{pre}|)/SNR_{pre}$.

Characterization

Transmission electron microscopy (TEM) and high-resolution TEM (HRTEM) images were obtained by using a JEM-2100 microscope with an accelerating voltage of 200 kV. The X-ray diffraction (XRD) patterns were acquired on a Rigaku Ultima IV system. The energy-dispersive X-ray (EDX) element mapping analysis was performed on a Tecnai F30 microscope at an accelerating voltage of 300 kV. The hysteresis loops (at 300 K) were recorded on a Quantum Design MPMS-XL-7 system. The samples ready for magnetization measurement were washed three times and then treated with plasma cleaning (PDC-32G, Harrick Plasma) to remove the surfactants. The metal concentration of the samples was detected by inductively coupled plasma atomic emission spectroscopy (ICP-AES). The dynamic light scattering (DLS) measurements were performed on a Malvern Zetasizer nano ZS instrument.

Statistical analysis

Statistical analysis was performed using the Student's t-test for unpaired data and the diameter of as-synthesized nanoparticles was calculated using Image J.

Results and discussion

We used iron oleate and europium oleate as precursors to prepare EuIO nanocubes in 1-octadecene solvent in the presence of oleic acid, which is different from the reported method of preparing europium doped iron oxide nanoparticles using ferric acetylacetonate and europium acetylacetonate as precursors.[34] We were able to tune the size of EuIO nanoparticles by varying the reaction time. The EuIO nanocubes with the sizes of 10, 14 and 20 nm in diameter were synthesized with reflux times of 1, 1.5 and 2 hours, respectively (Fig. 1a–c). Transmission electron microscopy (TEM) images showed that they are of uniform cubic shape with narrow size distribution. After coating with sodium citrate, dynamic light scattering (DLS) analysis indicated that they are stable in water with hydrodynamic diameters of 10.0 ± 1.7, 14.0 ± 1.9, and 20.1 ± 2.4 nm, respectively (Fig. 1d–f). EuIO nanocubes with different Eu molar ratios (6.4%, 10.3% and 15.1%) were also prepared by tuning the proportions of the two precursors (ESI, Fig. S1†). High-resolution TEM (HRTEM) image of the 14 nm sized EuIO nanocubes (Fig. 2a, inset) reveals a crossed lattice spacing distance of about 2.9 Å corresponding to (220) planes of the Fe_3O_4 crystal. The energy-dispersive X-ray (EDX) line scanning analysis and element mapping indicate that Eu(III) ions are homogeneously distributed in iron oxide nanoparticles (Fig. 2d,e). X-ray diffraction (XRD) patterns showed mixed diffraction peaks of inverse spinel structures of magnetite (JCPDS

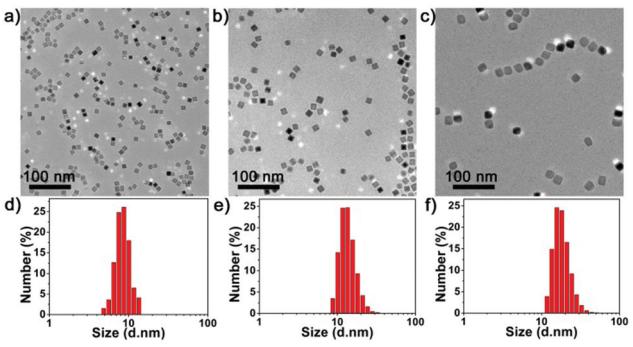

Fig. 1 TEM images (a–c) and the related DLS analysis profiles (d–f) of monodispersed EuIO nanocubes with different sizes: (a, d) 10.0 ± 1.7 nm, (b, e) 14.0 ± 1.9 nm, and (c, f) 20.1 ± 2.4 nm.

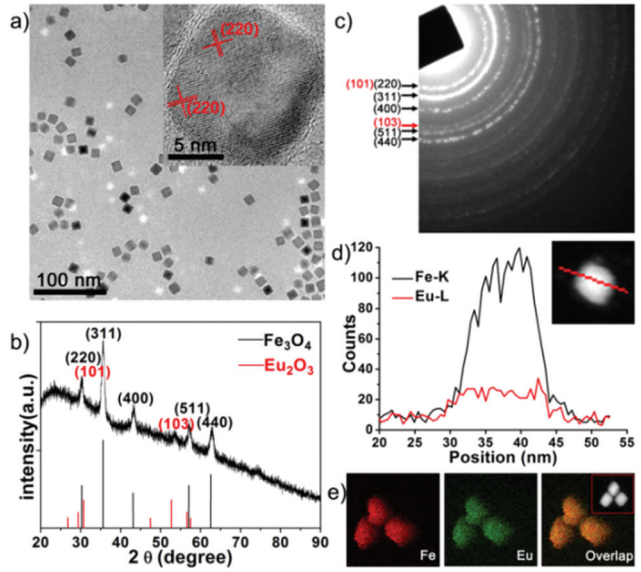

Fig. 2 Characterization of EuIO nanocubes. (a) Representative TEM image of 14 nm sized monodispersed EuIO nanocubes (inset: HRTEM image). (b) XRD and (c) SEAD patterns of EuIO nanocubes. (d) EDX line profiles across a EuIO nanocube (inset: a scanning TEM image with high angle annular dark field, STEM-HAADF image). (e) EDX mapping images of EuIO nanocubes (inset: STEM-HAADF image of relative EuIO nanocubes).

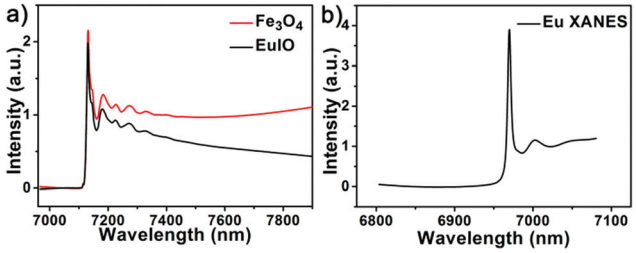

Fig. 3 (a) Fe K-edge XAS spectra of EuIO nanocubes and Fe_3O_4 nanoparticles, (b) Eu L_{III}-edge XAS spectrum of EuIO nanocubes. The absorption peaks are attributed to the $2p_{3/2}$/5d electron transition for the trivalent Eu L_{III}-edges.

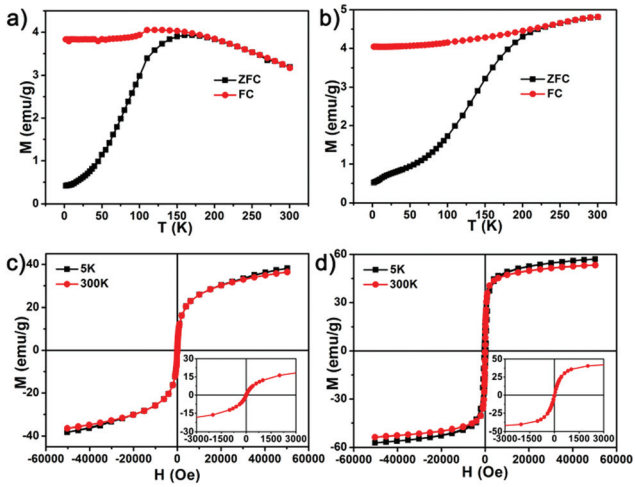

Fig. 4 Magnetic properties. Temperature dependent magnetization curves under ZFC/FC conditions of (a) EuIO nanocubes and (b) magnetite nanoparticles under an applied magnetic field of 50 Oe. Field-dependent magnetization curves (M–H) of (c) EuIO nanocubes and (d) magnetite nanoparticles at 300 K and 5 K (insets: magnification of M–H curves from −3000 to 3000 Oe at 300 K).

no. 00-003-0863) and hexagonal Eu_2O_3 (JCPDS no. 00-019-0463) phases (Fig. 2b). The selected area electron diffraction (SAED) of EuIO nanoparticles also exhibited a mixed crystalline nature (Fig. 2c). These results are different from that of either the doped ferrites with inverse or normal spinel crystalline structures,[15,35] indicating that EuIO nanocubes are composed of mixed magnetite and Eu_2O_3 nanoclusters. This phenomenon is probably due to the fact that the large size of Eu(III) ions (94.7 pm in radius) is unable to occupy either the tetrahedral or the octahedral interstitial sites in the spinel structure. We also used synchrotron X-ray absorption spectroscopy (XAS) to further envision the structure of EuIO nanocubes, which allows for analyzing coordination geometry, bonding environment, and the electronic structure of central atoms.[36] The Fe K-edge XAS spectra of EuIO nanocubes are comparable to those of Fe_3O_4 nanoparticles (Fig. 3a), indicating that the inverse spinel structure of Fe_3O_4 was unaltered after Eu_2O_3 embedding. However, the peak intensity of the EuIO sample is lower than that of the Fe_3O_4 nanoparticles, suggesting that the embedded Eu_2O_3 nanoclusters may disturb the long range order of spins of iron oxide nanoparticles. The absorption peaks of the Eu L_{III}-edge XAS spectrum of EuIO nanocubes (Fig. 3b) are attributed to the $2p_{3/2}$/5d electron transition for the trivalent Eu L_{III}-edges, indicating typical Eu(III) characteristics.[37–39]

Standard zero-field cooling (ZFC) and field cooling (FC) measurements for EuIO nanocubes (Fig. 4a) showed the estimated blocking temperature of about 180 K, which are lower than 220 K for magnetite nanoparticles (Fig. 4b). The hysteresis loops (M–H) revealed that EuIO nanocubes are partially paramagnetic without magnetic hysteresis at 300 K, which is different from the superparamagnetic behaviors of magnetite nanoparticles (Fig. 4c,d, and insets). This phenomenon is probably attributed to the enhanced spin canting effect on the surface layer of EuIO nanocubes after Eu_2O_3 embedding due to the enhanced thermal agitation effect.[40] The inner location of Eu_2O_3 clusters in iron oxide nanoparticles may disturb the local magnetic field intensity of the whole nanoparticle and finally reduce the saturated magnetization (M_s). Besides, the doping of Eu_2O_3 with low magnetization may also decrease the total M_s values of EuIO nanocubes.[41] As a result, the M_s value of EuIO nanocubes (~39.6 emu g^{-1}) is lower than that of magnetite nanoparticles with a similar size (~53.4 emu g^{-1}) at 300 K.

To evaluate the MR contrast ability of EuIO nanocubes, we firstly measured the relaxivities of citrate coated EuIO samples with different sizes and different Eu molar ratios. Larger EuIO nanoparticles have relatively higher M_s values, which can be attributed to the loss of the predominant spin canting effect on the particle surface.[42–44] Nanoparticles with higher M_s values may generate stronger local magnetic field inhomogeneities for the water proton dephasing process around the nanoparticles according to the quantum mechanical outer sphere theory.[45,46] As a result, larger EuIO nanocubes have higher r_1 and r_2 values (Fig. S3 and Table S1†). The Eu molar ratio also plays an important role in the r_1 and r_2 values of EuIO nanocubes, raising the Eu molar ratio increases r_1 values while reducing r_2 values (Fig. S4†). The decrease of r_2 values is probably due to the reduction of the M_s values after Eu embedding. The increased r_1 value may be attributed to the spin order of Eu(III) which has the same orientation as the local magnetic field.[31] However, when the Eu molar ratio reached 15.1%, both r_1 and r_2 values are diminished, which may be ascribed to the structure of Fe_3O_4 nanoparticles disturbed severely by a large amount of Eu_2O_3 nanoclusters (Table S2†).

We also prepared Fe_3O_4 and Eu_2O_3 nanoparticles with about 14 nm in diameter for comparison (Fig. S2†). EuIO nanocubes showed increased signals in T_1-weighted MR images (Fig. 5a) and reduced signals in T_2-weighted MR images (Fig. 5b) with increased metal concentrations. Fe_3O_4 nanoparticles gave reduced signals in T_2-weighted MR images but there were no obvious signal changes in T_1-weighted MR images. Eu_2O_3 nanoparticles showed no evidence of signal changes both in T_1- and T_2-weighted MR images. The r_1 value of EuIO nanocubes is 36.79 ± 1.16 mM^{-1} s^{-1}, which is much higher than that of Fe_3O_4 nanoparticles (12.47 ± 0.32 mM^{-1} s^{-1}) and Eu_2O_3 nanoparticles (0.03 ± 0.01 mM^{-1} s^{-1}) (Fig. 5c and S5†). The increased r_1 value is probably due to the spin order of Eu(III) which has the same direction as the local magnetic field induced by the superparamagnetic iron oxide domains. Besides, the chemical exchange of the surface Eu(III) ions with the nearby water protons may enhance T_1 shortening compared with iron ions. The r_2 of EuIO nanocubes was 97.52 ± 2.16 mM^{-1} s^{-1}, which is much higher than that of Eu_2O_3 nanoparticles (5.44 ± 0.12 mM^{-1} s^{-1}) but slightly lower than Fe_3O_4 nanoparticles (116.78 ± 3.77 mM^{-1} s^{-1}), which is probably due to the relatively low M_s value. It is well-known that the r_2/r_1 ratio is an important factor to estimate whether a contrast agent can serve as a T_1 or T_2 contrast agent.[47] A low r_2/r_1 ratio is necessary for magnetic nanoparticles to show the T_1 contrast enhancement effect.[28,48] The 14 nm sized EuIO nanocubes showed a low r_2/r_1 value, together with a relatively high r_2 value (Fig. 5c), further confirming that EuIO nanocubes may possess the T_1–T_2 dual-modal MR contrast ability.

We evaluated the cytotoxicity of EuIO nanoparticles using the tetrazolium-based colorimetric (MTT) assay. After incubating with SMMC-7721 cells or MRC-5 cells, there was scarcely any cytotoxicity even at the highest metal ion concentration (120 μg [Fe + Eu] mL^{-1}), indicating good biocompatibility of the sodium citrate-coated EuIO nanocubes (Fig. S6†). To test

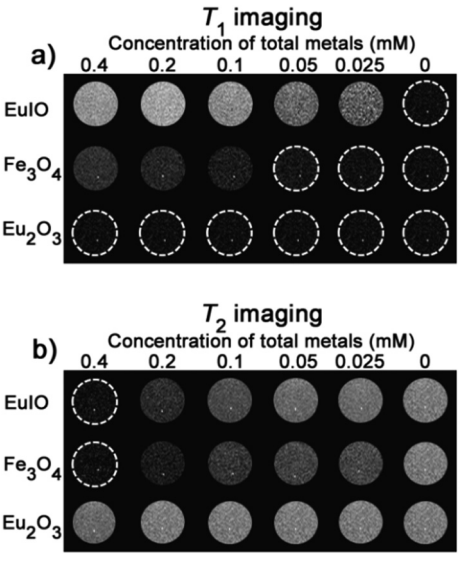

c)

Nanoparticles	r_1($mM^{-1}s^{-1}$)	r_2($mM^{-1}s^{-1}$)	r_2/r_1
EuIO-14	36.79 ± 1.16	97.52 ± 2.16	2.65
Fe_3O_4-14	12.47 ± 0.32	116.78 ± 3.77	9.36
Eu_2O_3-14	0.03 ± 0.01	5.44 ± 0.12	181

Fig. 5 MRI contrast enhancement performance of EuIO nanocubes compared to Fe_3O_4 and Eu_2O_3 nanoparticles with similar sizes of about 14 nm. (a) T_1-weighted and (b) T_2-weighted phantom imaging of 14 nm sized EuIO nanocubes, magnetite and Eu_2O_3 nanoparticles on a 0.5 T MRI scanner. (c) The r_1 and r_2 values of EuIO nanocubes, Fe_3O_4 and Eu_2O_3 nanoparticles.

the MRI contrast ability of the EuIO nanocubes *in vitro*, we incubated SMMC-7721 cells with EuIO nanocubes and Fe_3O_4 nanoparticles at different concentrations (0.2, 0.4, and 0.8 mM of total metal ions). The cellular uptake amounts of EuIO nanocubes and Fe_3O_4 nanoparticles are similar at equivalent total metal concentrations (Fig. S7†). As shown in Fig. 6a, cells after being incubated with EuIO nanocubes showed brighter signals in T_1 imaging in comparison with Fe_3O_4 nanoparticle treated cells. The signal to noise ratios in T_1 imaging further confirmed that the EuIO nanocubes group is much higher than the Fe_3O_4 nanoparticles group (Fig. 6c). The ΔSNR (ΔSNR = $|SNR_{post} - SNR_{pre}|/SNR_{pre}$) for cells incubated with EuIO nanocubes is 61.4 ± 5.3%, which is much larger than that of Fe_3O_4 nanoparticles (13.5 ± 4.5%) in the concentration of 0.8 mM (Table S3†), demonstrating that EuIO nanocubes show better T_1-weighted MR contrast enhancement effect than Fe_3O_4 nanoparticles. In T_2-weighted MR imaging, the signal intensity of cells after being incubated with EuIO nanocubes and Fe_3O_4 nanoparticles were both decreased along with the augment of concentrations (Fig. 6b). The signal changes in the EuIO nanocubes group are close to those in the Fe_3O_4 nanoparticles group (Fig. 6d and Table S4†). These results prove

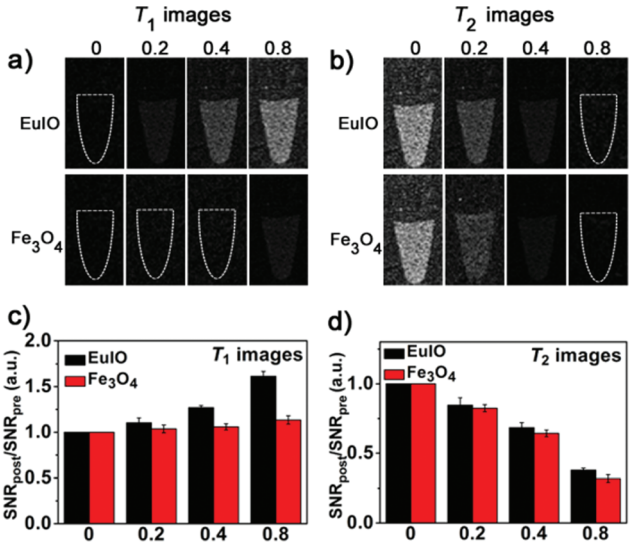

Fig. 6 T_1 and T_2 contrast-enhanced MRI of cancer cells *in vitro*. (a) T_1- and (b) T_2-weighted MR images of SMMC-7721 cells before and after incubated with 0.8, 0.4 and 0.2 mM EuIO nanocubes and Fe_3O_4 nanoparticles (with respect to total metals). Cells treated with EuIO nanocubes showed both T_1 and T_2 contrast enhanced effects, but the group treated with Fe_3O_4 nanoparticles only showed a T_2 contrast enhanced effect. MR signal-to-noise ratio (SNR) changes of (c) T_1 images and (d) T_2 images.

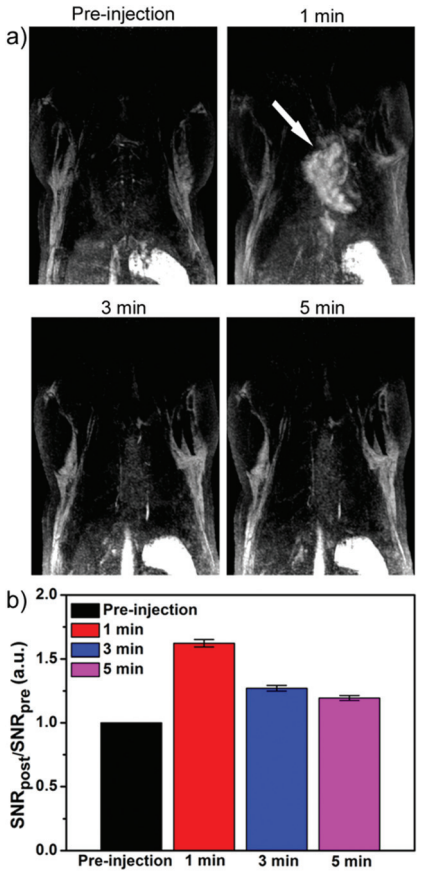

Fig. 7 *In vivo* T_1-weighted MR imaging of mice at the coronal plane and the related quantificational analysis of signal changes. (a) T_1-weighted MR images at 0, 1, 3, and 5 min post-intravenous injection of 14 nm sized EuIO nanocubes with a dose of 2 mg (Eu + Fe) per kg of body weight, a white arrow shows the region of interest, heart. (b) Quantification of signal changes (SNR_{post}/SNR_{pre}) in the heart at different time points after administration (n = 3 per group).

that EuIO nanocubes show both T_1 and T_2 contrast effects *in vitro*, indicating the potential of EuIO nanocubes as T_1–T_2 dual-modal contrast agents.

We then performed the animal experiments using healthy Sprague–Dawley rats as models for *in vivo* MRI studies. The T_1-weighted MR images at 3 T were obtained sequentially before and after intravenous injection of EuIO nanocubes with a dose of 2 mg [Fe + Eu] per kg of body weight (Fig. 7a). The heart exhibited a significantly brighter signal at 1 min time point post-injection (p.i.) and the ΔSNR was approximately 62.2% (Fig. 7b and Table S5†), which indicates a great potential of EuIO nanocubes as excellent T_1 contrast agents *in vivo*. Because nanoparticles are highly accumulated in the hepatic Kupffer cells of the liver due to the mononuclear phagocyte system (MPS),[49,50] we then focused on the liver as the region of interest (ROI). The T_2-weighted MR images at a 3 T MR scanner showed prominent T_2 contrast in the rat liver region after intravenous injection of EuIO nanoparticles with a dose of 2.0 mg [Fe + Eu] per kg of body weight (Fig. 8). The analysis of MR signal changes in the liver region indicated that the maximal ΔSNR is about 77.3% at 90 min p.i. at 3 T (Fig. 8b and Table S6†). This result suggests that EuIO nanocubes have robust contrast effects for liver imaging with a diagnostic time window in two hours after intravenous administration, indicating a relatively long blood circulation time.[51] The animal experiments demonstrate that EuIO nanoparticles are able to show both T_1 and T_2 MRI contrast effects for an *in vivo* study, which may provide more useful information for diagnosis with enhanced accuracy.

Conclusions

In summary, we have demonstrated that EuIO nanocubes showed both T_1 and T_2 contrast enhancement effects *in vitro* and *in vivo*. Moreover, we can tune T_1 and T_2 contrast abilities by varying their sizes and Eu doping ratios, which is helpful to better understand the effects of size and doping on r_1 and r_2 values and rationally design T_1–T_2 dual-modal MRI contrast agents. The synthesis of EuIO nanocubes is facile, highly reproducible, and convenient to scale up. The sodium citrate coated EuIO nanocubes displayed good biocompatibility and a relative long blood circulation time. These desirable characters render them as a promising candidate for T_1- and T_2-weighted contrast-enhanced MRI, which may provide a feasible strategy for accurate detection of lesions in future. The EuIO nanocubes may also bind with other biomolecules (*e.g.*, antibody and peptides), thereby providing a versatile platform for targeting and self-confirmed imaging for biomedical applications.

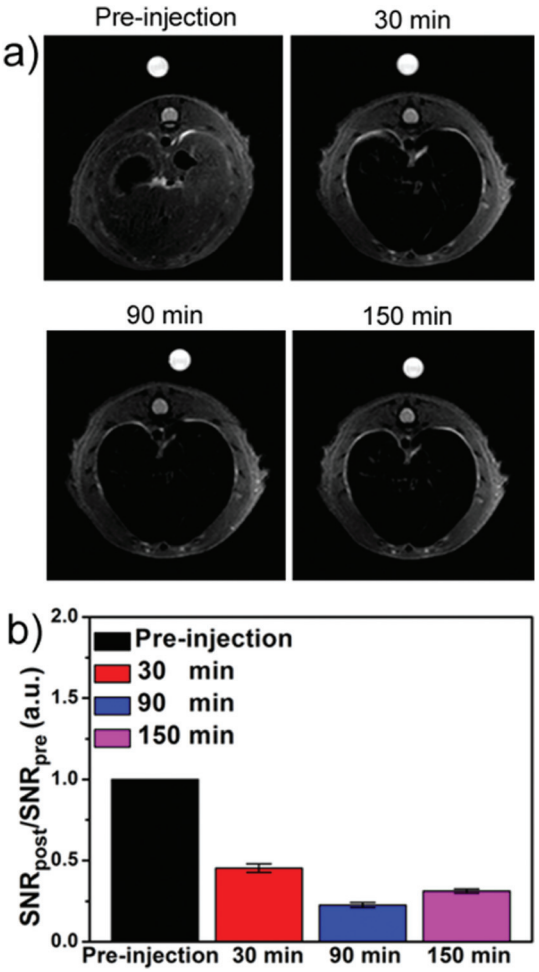

Fig. 8 *In vivo* T_2-weighted MR imaging of the liver at the transverse plane and the related quantificational analysis of signal changes. (a) T_2-weighted MR images of mice before and after intravenous injection of EuIO nanocubes at 3 T with a dose of 2 mg (Eu + Fe) per kg of mouse body weight. (b) Quantitative analysis of signal changes (SNR ratio) in the liver at different time points after administration (n = 3 per group).

Acknowledgements

This work was supported by the National Key Basic Research Program of China (2013CB933900, 2014CB744502, and 2014CB932004), National Natural Science Foundation of China (21222106, 81370042, and 81430041), Natural Science Foundation of Fujian (2013J06005), and Fok Ying Tung Education Foundation (142012). We thank Prof. X. Guan at Tongji University and Shanghai Synchrotron Radiation Facility for XAS analysis.

Notes and references

1 N. Lee and T. Hyeon, *Chem. Soc. Rev.*, 2012, **41**, 2575–2589.
2 C. Tassa, S. Y. Shaw and R. Weissleder, *Acc. Chem. Res.*, 2011, **44**, 842–852.
3 J. Gao, H. Gu and B. Xu, *Acc. Chem. Res.*, 2009, **42**, 1097–1107.
4 D. Ho, X. Sun and S. Sun, *Acc. Chem. Res.*, 2011, **44**, 875–882.
5 T. D. Schladt, K. Schneider, H. Schild and W. Tremel, *Dalton Trans.*, 2011, **40**, 6315–6343.
6 H. Yang, Y. Zhuang, Y. Sun, A. Dai, X. Shi, D. Wu, F. Li, H. Hu and S. Yang, *Biomaterials*, 2011, **32**, 4584–4593.
7 J. Y. Park, M. J. Baek, E. S. Choi, S. Woo, J. H. Kim, T. J. Kim, J. C. Jung, K. S. Chae, Y. Chang and G. H. Lee, *ACS Nano*, 2009, **3**, 3663–3669.
8 H. B. Na, J. H. Lee, K. An, Y. I. Park, M. Park, I. S. Lee, D.-H. Nam, S. T. Kim, S.-H. Kim, S.-W. Kim, K.-H. Lim, K.-S. Kim, S.-O. Kim and T. Hyeon, *Angew. Chem., Int. Ed.*, 2007, **119**, 5493–5497.
9 W. J. Rieter, K. M. L. Taylor, H. An, W. Lin and W. Lin, *J. Am. Chem. Soc.*, 2006, **128**, 9024–9025.
10 G. Huang, J. Hu, H. Zhang, Z. Zhou, X. Chi and J. Gao, *Nanoscale*, 2014, **6**, 726–730.
11 Z. Zhao, Z. Zhou, J. Bao, Z. Wang, J. Hu, X. Chi, K. Ni, R. Wang, X. Chen, Z. Chen and J. Gao, *Nat. Commun.*, 2013, **4**, 2266.
12 J. Gallo, N. J. Long and E. O. Aboagye, *Chem. Soc. Rev.*, 2013, **42**, 7816–7833.
13 S. Cheong, P. Ferguson, K. W. Feindel, I. F. Hermans, P. T. Callaghan, C. Meyer, A. Slocombe, C.-H. Su, F.-Y. Cheng, C.-S. Yeh, B. Ingham, M. F. Toney and R. D. Tilley, *Angew. Chem., Int. Ed.*, 2011, **123**, 4292–4295.
14 J. Yang, C.-H. Lee, H.-J. Ko, J.-S. Suh, H.-G. Yoon, K. Lee, Y.-M. Huh and S. Haam, *Angew. Chem., Int. Ed.*, 2007, **46**, 8836–8839.
15 J.-H. Lee, Y.-M. Huh, Y.-w. Jun, J.-w. Seo, J.-t. Jang, H.-T. Song, S. Kim, E.-J. Cho, H.-G. Yoon, J.-S. Suh and J. Cheon, *Nat. Med.*, 2007, **13**, 95–99.
16 B. H. Kim, N. Lee, H. Kim, K. An, Y. I. Park, Y. Choi, K. Shin, Y. Lee, S. G. Kwon, H. B. Na, J.-G. Park, T.-Y. Ahn, Y.-W. Kim, W. K. Moon, S. H. Choi and T. Hyeon, *J. Am. Chem. Soc.*, 2011, **133**, 12624–12631.
17 E. Terreno, D. D. Castelli, A. Viale and S. Aime, *Chem. Rev.*, 2010, **110**, 3019–3042.
18 C.-L. Liu, Y.-K. Peng, S.-W. Chou, W.-H. Tseng, Y.-J. Tseng, H.-C. Chen, J.-K. Hsiao and P.-T. Chou, *Small*, 2014, **10**, 3962–3969.
19 U. I. Tromsdorf, O. T. Bruns, S. C. Salmen, U. Beisiegel and H. Weller, *Nano Lett.*, 2009, **9**, 4434–4440.
20 Z. Zhou, L. Wang, X. Chi, J. Bao, L. Yang, W. Zhao, Z. Chen, X. Wang, X. Chen and J. Gao, *ACS Nano*, 2013, **7**, 3287–3296.
21 H. Kobayashi, M. R. Longmire, M. Ogawa and P. L. Choyke, *Chem. Soc. Rev.*, 2011, **40**, 4626–4648.
22 P. Caravan, *Acc. Chem. Res.*, 2009, **42**, 851–862.
23 R. B. Lauffer, *Chem. Rev.*, 1987, **87**, 901–927.
24 G. Huang, H. Li, J. Chen, Z. Zhao, L. Yang, X. Chi, Z. Chen, X. Wang and J. Gao, *Nanoscale*, 2014, **6**, 10404–10412.
25 J. Y. Park, E. S. Choi, M. J. Baek, G. H. Lee, S. Woo and Y. Chang, *Eur. J. Inorg. Chem.*, 2009, **17**, 2477–2481.

26 K. Cheng, M. Yang, R. Zhang, C. Qin, X. Su and Z. Cheng, *ACS Nano*, 2014, **8**, 9884–9896.
27 J.-s. Choi, J.-H. Lee, T.-H. Shin, H.-T. Song, E. Y. Kim and J. Cheon, *J. Am. Chem. Soc.*, 2010, **132**, 11015–11017.
28 Z. Zhou, Z. Zhao, H. Zhang, Z. Wang, X. Chen, R. Wang, Z. Chen and J. Gao, *ACS Nano*, 2014, **8**, 7976–7985.
29 W. Xu, B. A. Bony, C. R. Kim, J. S. Baeck, Y. Chang, J. E. Bae, K. S. Chae, T. J. Kim and G. H. Lee, *Sci. Rep.*, 2013, **3**, 3210.
30 X. Wang, Z. Zhou, Z. Wang, Y. Xue, Y. Zeng, J. Gao, L. Zhu, X. Zhang, G. Liu and X. Chen, *Nanoscale*, 2013, **5**, 8098–8104.
31 Z. Zhou, D. Huang, J. Bao, Q. Chen, G. Liu, Z. Chen, X. Chen and J. Gao, *Adv. Mater.*, 2012, **24**, 6223–6228.
32 K. Kattel, J. Y. Park, W. Xu, H. G. Kim, E. J. Lee, B. A. Bony, W. C. Heo, J. J. Lee, S. Jin, J. S. Baeck, Y. Chang, T. J. Kim, J. E. Bae, K. S. Chae and G. H. Lee, *ACS Appl. Mater. Interfaces*, 2011, **3**, 3325–3334.
33 J. Park, K. An, Y. Hwang, J.-G. Park, H.-J. Noh, J.-Y. Kim, J.-H. Park, N.-M. Hwang and T. Hyeon, *Nat. Mater.*, 2004, **3**, 891–895.
34 C. R. De Silva, S. Smith, I. Shim, J. Pyun, T. Gutu, J. Jiao and Z. Zheng, *J. Am. Chem. Soc.*, 2009, **131**, 6336–6337.
35 J.-t. Jang, H. Nah, J.-H. Lee, S. H. Moon, M. G. Kim and J. Cheon, *Angew. Chem., Int. Ed.*, 2009, **121**, 1260–1264.
36 T. E. Westre, P. Kennepohl, J. G. DeWitt, B. Hedman, K. O. Hodgson and E. I. Solomon, *J. Am. Chem. Soc.*, 1997, **119**, 6297–6314.
37 F. A. Rabuffetti, S. P. Culver, J. S. Lee and R. L. Brutchey, *Nanoscale*, 2014, **6**, 2909–2914.
38 M. Lastusaari, H. F. Brito, S. Carlson, J. Hölsä, T. Laamanen, L. C. V. Rodrigues and E. Welter, *Phys. Scr.*, 2014, **89**, 044004.
39 K. Takashi, H. Tetsuo, O. Koutoku, O. Susumu and O. Hitoshi, *Jpn. J. Appl. Phys.*, 2013, **52**, 042402.
40 M. P. Morales, S. Veintemillas-Verdaguer, M. I. Montero, C. J. Serna, A. Roig, L. Casas, B. Martínez and F. Sandiumenge, *Chem. Mater.*, 1999, **11**, 3058–3064.
41 H. B. Na, I. C. Song and T. Hyeon, *Adv. Mater.*, 2009, **21**, 2133–2148.
42 E. D. Smolensky, H.-Y. E. Park, Y. Zhou, G. A. Rolla, M. Marjanska, M. Botta and V. C. Pierre, *J. Mater. Chem. B*, 2013, **1**, 2818–2828.
43 J. V. Jokerst and S. S. Gambhir, *Acc. Chem. Res.*, 2011, **44**, 1050–1060.
44 Y.-w. Jun, Y.-M. Huh, J.-s. Choi, J.-H. Lee, H.-T. Song, K. Kim, S. Yoon, K.-S. Kim, J.-S. Shin, J.-S. Suh and J. Cheon, *J. Am. Chem. Soc.*, 2005, **127**, 5732–5733.
45 Q. L. Vuong, J.-F. Berret, J. Fresnais, Y. Gossuin and O. Sandre, *Adv. Healthcare Mater.*, 2012, **1**, 502–512.
46 D. Yoo, J.-H. Lee, T.-H. Shin and J. Cheon, *Acc. Chem. Res.*, 2011, **44**, 863–874.
47 P. Caravan, J. J. Ellison, T. J. McMurry and R. B. Lauffer, *Chem. Rev.*, 1999, **99**, 2293–2352.
48 Y.-K. Peng, C.-L. Liu, H.-C. Chen, S.-W. Chou, W.-H. Tseng, Y.-J. Tseng, C.-C. Kang, J.-K. Hsiao and P.-T. Chou, *J. Am. Chem. Soc.*, 2013, **135**, 18621–18628.
49 J. Huang, L. Bu, J. Xie, K. Chen, Z. Cheng, X. Li and X. Chen, *ACS Nano*, 2010, **4**, 7151–7160.
50 J. Gao, K. Chen, R. Xie, J. Xie, S. Lee, Z. Cheng, X. Peng and X. Chen, *Small*, 2010, **6**, 256–261.
51 K. P. García, K. Zarschler, L. Barbaro, J. A. Barreto, W. O'Malley, L. Spiccia, H. Stephan and B. Graham, *Small*, 2014, **10**, 2516–2529.